Materials Research Express

PAPER • OPEN ACCESS

Tribocorrosion behaviors of TiSiCN nanocomposite coatings deposited by high power impulse magnetron sputtering

To cite this article: Haoqi Wang *et al* 2020 *Mater. Res. Express* **7** 076407

Materials Research Express

PAPER

Tribocorrosion behaviors of TiSiCN nanocomposite coatings deposited by high power impulse magnetron sputtering

Haoqi Wang[1], **Yixiang Ou**[2,3,6], **Xu Zhang**[1], **Bin Liao**[1], **Xuedong Ou**[4], **Jun Luo**[2], **Pan Pang**[2], **Lin Chen**[2], **Qingsong Hua**[1,6] **and Manyu Bao**[5]

[1] Key Laboratory of Beam Technology of Ministry of Education, College of Nuclear Science and Technology, Beijing Normal University, Beijing 100875, People's Republic of China
[2] Beijing Radiation Center, Beijing Academy of Science and Technology, Beijing 100875, People's Republic of China
[3] Department of Biological Engineering, Changzhi Medical College, Changzhi 046000, People's Republic of China
[4] National key Laboratory of Science and Technology on Reliability and Environmental Engineering, Beijing Institute of Spacecraft Environment Engineering, Beijing 100094, People's Republic of China
[5] Beijing Jinlunkuntian Special Machine Co. Ltd Beijing 100085, People's Republic of China
[6] Authors to whom any correspondence should be addressed.

E-mail: ouyx16@tsinghua.org.cn **and** q.hua@bnu.edu.cn

Keywords: TiSiCN nanocomposite coatings, high power impulse magnetron sputtering, superhardness, tribocorriosion properties

OPEN ACCESS

RECEIVED
21 February 2020

REVISED
9 May 2020

ACCEPTED FOR PUBLICATION
22 May 2020

PUBLISHED
17 July 2020

Abstract

High-performance coatings originated in ingenious coating designs and advanced preparation techniques are expected to fulfill imperious demands in propulsion, bearings and mechanical seals, etc in marine systems for seawater lubrication. In this work, TiSiCN nanocomposite coatings were deposited by high power impulse magnetron sputtering at a power of 4–8 kW. As power is increased, TiSiCN coatings possess nanocrystalline (TiN, TiC, TiCN)/amorphous (Si_3N_4, SiC, sp^2-C) nanocomposite structure without distinctly preferred orientation. The highest hardness (H) of 43 GPa and effective Young's modulus (E^*) of 360 GPa were achieved at 8 kW, while the highest H/E^* of 0.123 and H^3/E^{*2} of 0.61 appear at 7 kW due to refined nano-grains, uniform distribution, high surface/interface integrity and fully dense microstructure. Rockwell C adhesion level increased from HF2 at 4 kW to HF1 at 8 kW. TiSiCN coatings with high H, H/E^*, H^3/E^{*2} and adhesion exhibit high open circuit potential of −0.07 V, low friction coefficient of 0.25 and specific wear rate of 4.78×10^{-5} $mm^3\ N^{-1}\ m^{-1}$, resulting from mild abrasive wear without the occurrence of pitting corrosion in 3.5 wt.% NaCl aqueous solution. Moreover, cycling tribocorrosion tests revealed that passive films possess strong abilities of regeneration and self-repairation on sliding contact surface.

1. Introduction

It is well known that stainless steel have been widely used in marine industry due to their good corrosion resistance. However, noteworthy is that surface treatment and protective coatings are always carried out to reach the combined improvement of wear and corrosion resistance owing to inferior tribocorrosion resistance of stainless steel [1–5]. There are extensive investigations on transition metal nitrides and diamond-like carbon (DLC) coatings deposited on stainless steel to improve tribocorrosion resistance of marine components. TiN and TiCN coatings deposited arc ion plating showed severe wear loss in artificial seawater compared to that of the coatings in air, distilled water [6]. It is found that TiCN coatings exhibited the best wear resistance in artificial seawater. Cr/graphite-like carbon multilayer coatings with various modulation periods by direct current magnetron sputtering had good tribocorrosion resistance in artificial seawater mainly thanks to contributions of the chemical inertness of amorphous carbon and interfaces in multilayer structure [7]. The adhesion of coatings to substrate also plays an important role in the tribocorrosion process in aggressive environments. Cr layer was deposited between substrate and coatings to significantly promote adhesion strength and wear resistance of GLC coatings [8].

It is generally believed that the tribocorrosion failure of hard coatings or films in seawater mainly originated from the friction-corrosion synergy interaction [9, 10]. The friction force induces plenty of fatigue micro-cracks, acting as the diffusion channels of Cl ions. The multi-scale Cl ion corrosion weakens the interfacial bonding strength resulting in coating failure [11]. Tribological hard coatings with high toughness exhibit high resistance to cracking during friction and wear process [12, 13]. It is found that ceramic coatings with high hardness and toughness can be achieved by the modulation of microstructure and defects in terms of interfaces, grain boundary, lattice distortion, etc [14–16]. Thus, hard coatings with high toughness can be achieved by coating design in terms of structure and multicomponent to enhance wear and corrosion resistance in seawater environments.

Novel coating designs and advanced preparation techniques play key roles in the performance of coated surface of components. It is well known that a conventional magnetron sputtering process always results in a porous microstructure owing to the low ionization density of target species [17], while vacuum arc processes are hard to eliminate micro-particles and porosity formed in coatings [18, 19]. High power impulse magnetron sputtering (HiPIMS) is also known as high-power pulsed magnetron sputtering (HPPMS), which can generate highly ionized target species with high density by applying a series of pulsed-power to target in a short period of time [20–23]. In our previous work, CrN/TiN superlattice coatings deposited by the combined deep oscillation magnetron sputtering and pulsed dc magnetron sputtering after the irradiation of high-intensity pulsed ion beams exhibited excellent tribocorrosion performance in seawater thanks to dense microstructure and high interface structure [24]. Therefore, in this work, TiSiCN nanocomposite coatings with Ti/TiSiC adhesion layers were deposited on AISI 316L stainless steel and Si (100) by HiPIMS at various target power of 4–8 kW. The effects of target power on tribocorrosion behaviors in 3.5 wt.% NaCl aqueous solution were investigated in details. The related tribocorrosion mechanism was discussed in terms of microstructure, adhesion strength, residual stress state, mechanical properties, electrochemical corrosion response. Eventually, TiSiCN nanocomposite coatings deposited by HiPIMS will bring forward a new concept of ingenious coating designs and advanced preparation techniques to fabricate advanced engineering surfaces to fulfill seawater lubrication ability for marine mechanical components in harsh environments.

2. Experimental details

2.1. Depositions of TiSiCN nanocomposite coatings

TiSiCN nanocomposite coatings with Ti/TiSiC adhesion layers were deposited on Si (100) and AISI 316L stainless steel coupons (20 mm × 20 mm × 3 mm) using high power impulse magnetron sputtering (HiPIMS) by sputtering Ti_3SiC_2 target in Ar/N_2 mixture gas at a power of 4–8 kW, where metal Ti and TiSiC layers serve as adhesion and transition layers, respectively. Si(100) substrates were used for structure and composition characterization of as-deposited coatings, while AISI 316L stainless steel for performance testing. TiSiC coatings were deposited by HiPIMS in Ar, while a Ti layer was sputtered as an adhesion layer by enhancing interfacial binding force between coating and substrate. The substrates were cleaned by acetone, absolute alcohol and deionized water in turn, and then were fixed on sample holder. Prior to the coating deposition, the samples were cleaned by Ar^+ ion etching at a bias voltage of 800 V for 10 min by gas ion source to remove any residual pollutants and the possible surface protective layer. Ti_3SiC_2 is well known for its high fracture toughness and high-temperature plasticity. It was deposited as an interface layer to reduce the concentration of thermal stress during film growth. Hence, the buffer layer formed by TiSiC and Ti layers is expected to support superhard TiSiCN coatings to reduce crack initiation and propagation [13].

TiSiCN nanocomposite coatings were composed of 3.1–3.7 μm thick TiSiCN coatings and 1.5 μm thick TiSiC/Ti buffer layers (TiSiC layer: 0.4 μm and Ti layer:1.1 μm). The pure Ti and Ti_3SiC_2 rectangular targets (449 mm × 75 mm × 6 mm) were oppositely installed in a cylindrical chamber (Φ 760 mm × 700 mm) to form closed field unbalanced magnetron sputtering system. The schematic diagram and HiPIMS pulse shapes of target current and voltage are shown in figure 1. The substrates were ultrasonically cleaned in acetone and anhydrous alcohol in turn and then were dried in nitrogen gas. Finally, they were fixed on the substrate holder. The distance between substrates and targets was kept at 100 mm. The chamber was pumped to the pressure of below 1×10^{-3} Pa. Before coatings deposition, all surfaces of substrates were cleaned using Ar gas ion source (2 kW, 150 kHz and pulse-on time 26 μs) at a flow rate of 120 sccm and substrate bias of −200 V for 20 min Ti adhesion layer with a thickness of 1.1 μm was firstly deposited on substrates using Advance Energy Pinnacle Plus power sources (2 kW, 150 kHz and pulse-on time 26 μs) at −50 V bias (Huettinger, Truplasma bias DC 4020 G2). And then, a 0.4 μm thick TiSiC coating was deposited using the HiPIMS plasma generator (Huettinger, Highpulse 4001 G2) by sputtering Ti_3SiC_2 compound target at a power of 4–8 kW and substrate bias of −60 V. Detailed deposition parameters are listed in table 1.

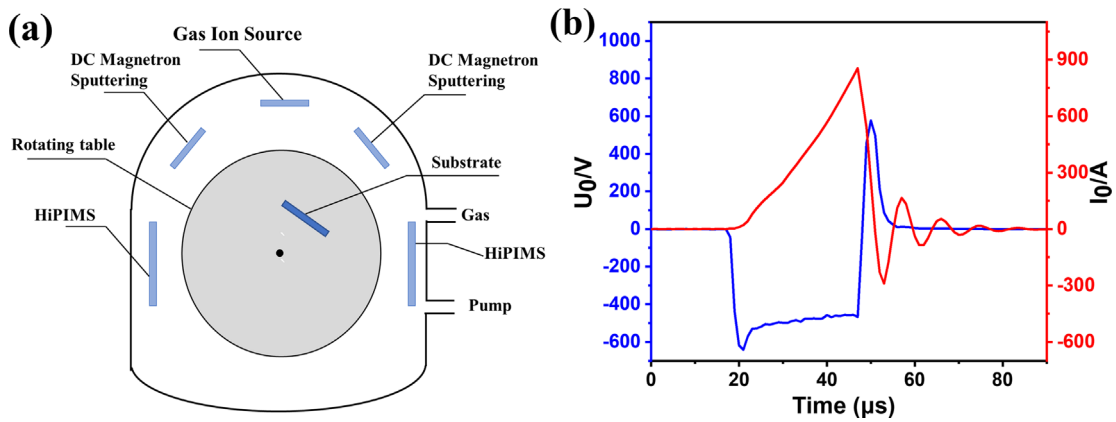

Figure 1. Schematic diagram and HiPIMS pulse shapes of target current and voltage.

Table 1. Typical process parameters, chemical composition and properties of TiSiCN nanocomposite coatings deposited by HiPIMS at various power.

Pa (kW)	f(Hz)	Depositon rate (nm min^{-1})	Residual stress (GPa)	Ra (nm)	Sa (nm)	OCP (V)	Specific wear rate (mm^{3}N^{-1}m^{-1})
4	280	25	−1.67	0.207	1.7	−0.12	1.54×10^{-4}
5	330	31	—	—	—	−0.10	7.42×10^{-5}
6	410	35	−2.03	0.292	1.01	−0.09	5.65×10^{-5}
7	480	49	—	—	—	−0.07	4.78×10^{-5}
8	540	47	−2.13	0.077	0.88	−0.08	5.53×10^{-5}

Note: P_a, target power; f, frequency; V_s, substrate bias; T_{sub}, substrate temperature; R_a/S_a, linear/surface roughness; OCP, open circuit potential. pulse width = 30μs U_{peak} = 280 ~ 310 V I_{peak} = 830 ~ 870 A.

2.2. Characterization of chemical composition and structure

X-ray photoelectron spectroscopy (XPS, ESCALAB250Xi, ThermoFisher) was performed to determine elemental composition and chemical bonding of coatings. X-ray diffraction (XRD, X'Pert PRO MPD, PANalytical) were used to detected phase composition and crystal structure of TiSiCN/TiSiC/Ti trilayer coatings. Field emission scanning electron microscopy (FESEM, S-4800, HITACHI) and transmission electron microscopy (TEM, Philips/FEI CM200) were carried out for investigations of cross-sectional morphologies and uniform in thickness. Atomic force microscope (AFM, Tosca 400, Anton Paar) was applied to detect linear roughness (Ra) and surface roughness (Sa) to characterize surface roughness. Also, surface morphology was observed. Film stress tester (FST1000) was used to measure residual stress state in coatings deposited on double-polished AISI 316L stainless steel wafers (50 mm × 10 mm × 0.8 mm), The computing method for residual stress is based on Stoney equation.

2.3. Mechanical properties and tribocorrosion behaviors

Hardness (H) and effective Young's modulus (E^*) of TiSiCN nanocomposite coatings were measured using a nanoindenter (Nanotest system, NanoTest, Micro Materials). Young's modulus of the coatings was calculated using the formula:

$$E^* = \frac{E}{1 - \nu^2} \tag{1}$$

Rockwell C indentation test (HRC) equipped with a 200 μm radius HRC indenter was used to evaluate adhesion of the coatings between AISI 316L stainless steel substrates. HRC adhesion level of coatings/substrates was determined according to FESEM images of Rockwell C indentations under a standard load of 150 kg [13]. Tribocorrosion performance of coatings was evaluated by a linear reciprocating tribometer integrated with a three-electrode cell configuration (MFT-EC4000, HUAHUI) against Si_3N_4 counterpart balls (Φ 6 mm) at a sliding time of 40 min. The tribocorrosion equipment and its schematic diagram are shown in figure 2. The constant reciprocating length was 5 mm in 3.5 wt.% NaCl aqueous solution. The normal load of 5 N and reciprocating frequency of 1 Hz were used for the coatings deposited at 4–8 kW and AISI 316L stainless steel substrate. Change of open circuit potential (OCP) as a function of sliding time was investigated to reveal the evolution of passive films during sliding wear tests. In order to clearly observe the *in situ* electrochemical

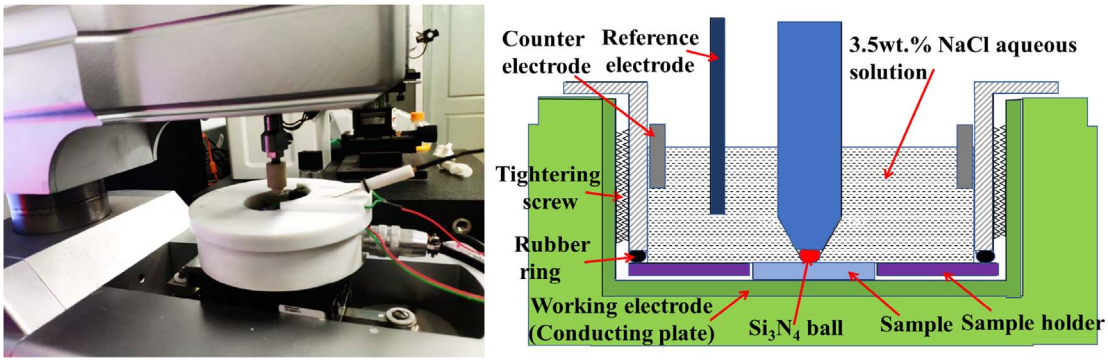

Figure 2. Tribocorrosion equipment and its schematic diagram.

response of the evolution of passive films, a larger normal load of 10 N and a slower frequency of 0.05 Hz was used in tribocorrosion tests for 60 min. Meanwhile, the regeneration and repairation of passive films on the sliding contact surfaces were studied in circulating tribocorrosion tests. The change of OCP in the start-stop process at every 10 min for 3 times was performed to study the periodic fluctuation of *in situ* electrochemical response of passive films. Wear tracks were carefully cleaned by deionized water. And then, Taylor Hobson surface profilometer was used to measure wear track profile to calculate specific tribocorrosion rates of worn samples. Further investigations on tribocorrosion mechanisms were carried out using FESEM and optical microscope images of worn surfaces.

3. Results and discussion

3.1. Chemical composition and microstructure

Mechanical components working in marine environments are required for their coated surface to possess excellent tribocorrosion properties [25]. Thus, high-performance coatings originated in ingenious coating designs and advanced preparation techniques are expected to fulfill imperious demands in terms of seawater lubrication, anti-corrosion and long lifetime. Hence, TiSiCN nanocomposite coatings were deposited by HiPIMS at a power of 4–8 kW, where metal Ti and TiSiC layers serve as adhesion and transition layers, respectively. Meanwhile, TiSiC and Ti layers constituted a TiSiC/Ti buffer layer. TiSiCN nanocomposite coatings are therefore expected to enhance carrying capacity, adhesion strength and tribocorrosion performance by controlling surface integrity, interface structure and microstructure under optimized HiPIMS plasma conditions.

Chemical composition and bonding state in the top surface layer of TiSiCN nanocomposite coatings were determined by XPS. With an increase of target power from 4 to 8 kW, Ti and N element content in TiSiCN coatings show an increase of 15.6–20.5 $\pm$ 1 at.% and 45.4–51.5 $\pm$ 2 at.%. There is a decrease of 13.8–11.3 $\pm$ 1 at.% and 25.2–16.7 $\pm$ 2 at.% for Si and C content, respectively. The O element content in TiSiCN coatings is less than 3 at.%, caused by surface oxide pollution. Figure 3 shows core-level XPS spectra of Ti2p, Si2p, C1s and N1s in TiSiCN nanocomposite coatings deposited by HiPIMS at a power of 4, 6 and 8 kW. At a low power of 4 kW, there are two main peaks in asymmetric Ti2p spectra, which is originated from $Ti2p_{3/2}$ and $Ti2p_{1/2}$ peaks in figure 3(a) at Binding energy (BE) of 455.6/461.6 eV. After peak-differentiating and imitating, it is clearly seen that four peaks at 455.1/460.7 eV, 456/461.6 eV, 456.9/462.9 eV and 458.4/464.0 eV reveal chemical bonds of Ti–C, Ti–N, Ti–O and Ti=O appear in TiSiCN coatings [25–28]. Ti–O and Ti=O bonds belong to surface oxides of Ti_2O_3 and TiO_2 phases [28–32]. Sigle peak at BE of 101.4 eV with broadening width in Si2p spectrum shows the existence of Si–C (101.1 eV) [26] and Si–N (101.8 eV) [16] bonds, as shown in figure 3(b). There are four peaks at 281.8 eV, 282.8 eV, 284.3 eV and 285.2 eV are overlapped to form a bigger peak in C1s spectrum in figure 3(c), possibly assigned to Ti–C, Si–C, sp^2–C and sp^3–C bonds [27–31]. Figure 3(d) presents that N1s spectrum contains a single peak at 397.1 eV, which are overlapped by two peaks at 397 eV and 398.3 eV belong to Ti–N and Si–N bonds [28]. With an increase of power, a slight increase of chemical bonds in Ti2p, Si2p and N1s, while a sharp feature of Ti–C bond peak is detected in C1s spectrum indicating the increase of chemical bonding of Ti–C in the coatings resulted from large amounts of ion species in HiPIMS plasma [20].

Figure 4 exhibits XRD patterns of TiSiCN nanocomposite coatings deposited on AISI 316L stainless steel substrates by HiPIMS at various target power. As shown in figure 4, (111), (200) and (222) diffraction peaks with broadening width overlapped by TiCN phases are detected in XRD patterns of coatings [29]. The peaks at 43.62°

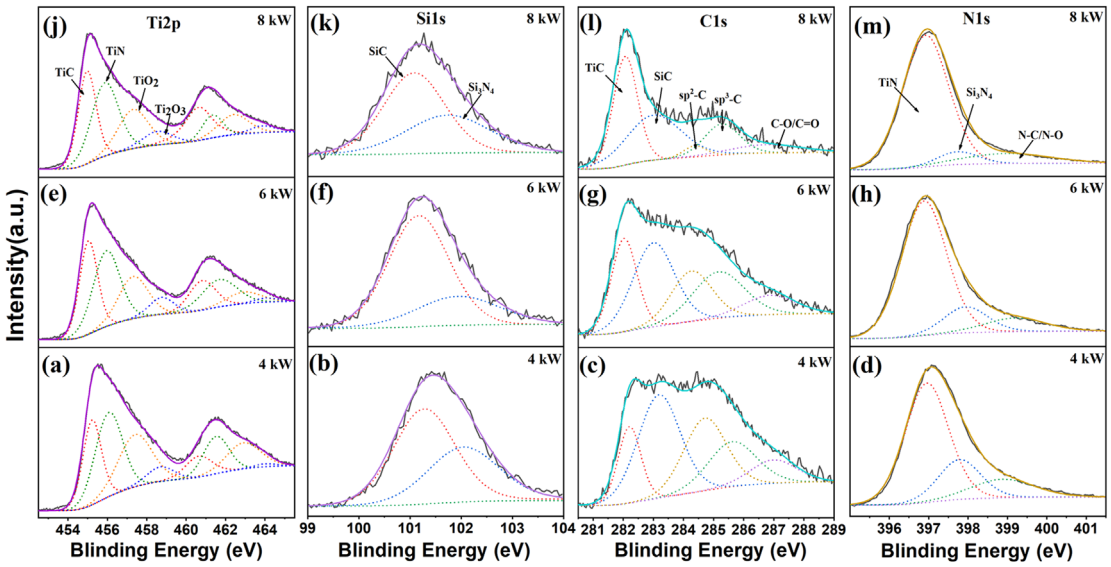

Figure 3. XPS spectra of TiSiCN nanocomposite coatings deposited by HiPIMS at various.

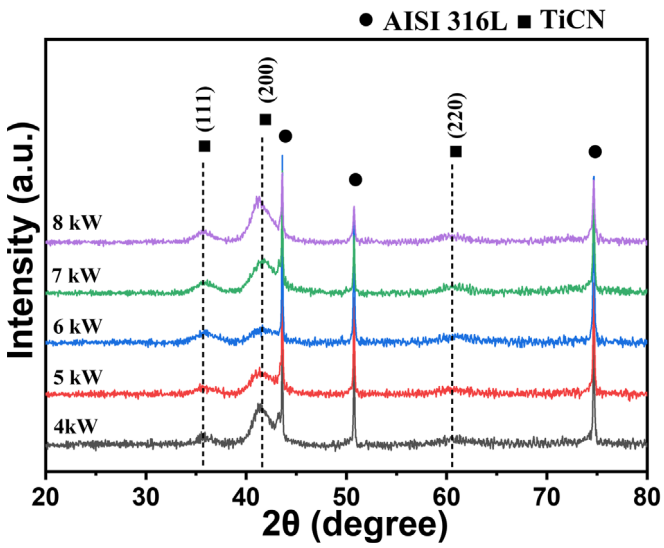

Figure 4. XRD patterns of TiSiCN nanocomposite coatings deposited on AISI 316L stainless steel substrates by HiPIMS at various target power.

and 50.70° are attributed to AISI 316L stainless steel substrate. Diffraction peaks from Ti–Si–C phase does not appear. Furthermore, the intensity factor ($f_{(hkl)}$) of diffraction peak, was calculated using the formula:

$$f_{(220)} = \frac{I_{(220)}}{I_{(220)} + I_{(111)} + I_{(200)}} \quad (2)$$

The $f_{(hkl)}$ firstly decreases from 84.4% at 4 kW to 49.2% at 6 kW, and then increases to 72.6% at 8 kW, agreed with the changes of TiN and TiC content in XPS patterns with an increasing target power of 4–8 kW. It is also indicated that the Ti–C–N phase was assigned to the superposition of TiN and TiC phases. With an increase in target power, the increased intensity and width of diffraction peaks indicate the decrease of the crystallinity. The plasma density increases with the increase of target power during deposition process, and the high-density bombardment of ion beam on the growth interface of the coating inhibits the growth of grains to result in grain refinement. According to XPS results, Si_3N_4, SiC and sp^2 carbon amorphous phases appear in the coatings. Hence, TiSiCN nanocomposite coatings are composed of nanocrystalline embedded in Si_3N_4, SiC and a few sp^2 carbon amorphous matrix. The composition and microstructure of TiSiCN coatings were influenced by carbon and nitrogen content [32]. Similar results are also reported by Wang *et al* [28] that special nanocomposite

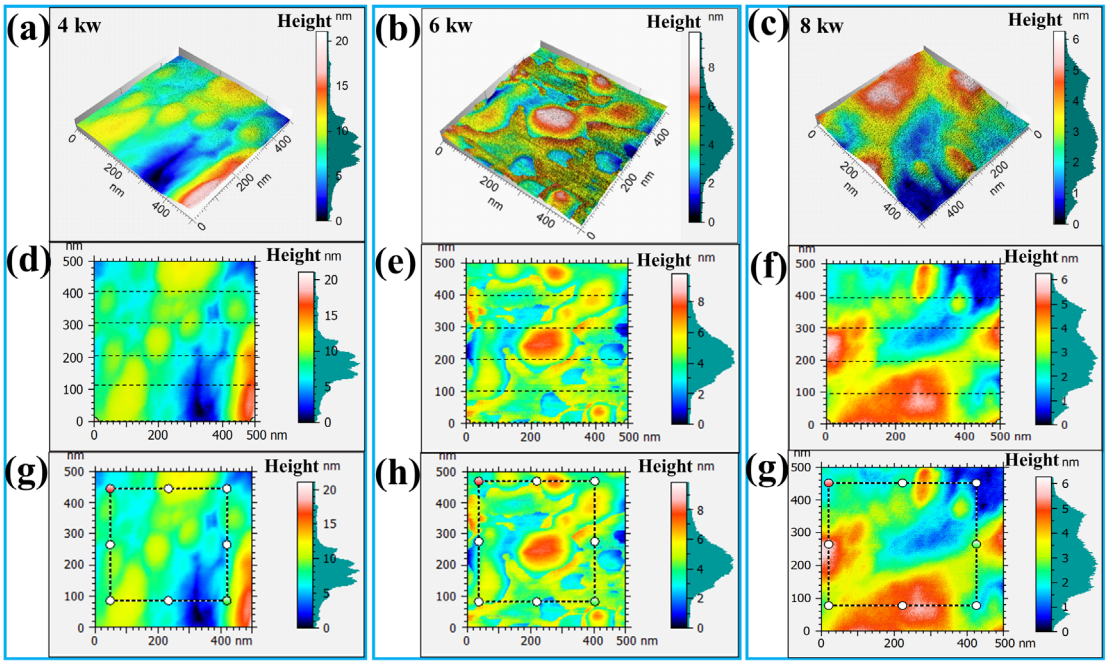

Figure 5. Surface morphology and roughness of TiSiCN nanocomposite coatings deposited by HiPIMS at various power.

structure of *nc*-(TiN, TiC and Ti(C,N))/*a*-(Si_3N_4, SiC and sp^2–C) are found in TiSiCN coatings with 11.9 wt.% C deposited using arc ion plating technique in Ar + C_2H_2 + N_2 mixture gases by sputtering TiSi target.

Surface integrity is associated with surface morphologies, surface roughness and microstructure of TiSiCN nanocomposite coatings. Top surface of coatings shows smooth feature without the formation of particles caused by arcing during reactive HiPIMS at 4–8 kW (figures 5(a)–(c)). Meanwhile, it is clearly seen in figures 5(d)–(f) that linear roughness of coatings increases from 0.207 to 0.292 nm, and then decrease to 0.077 nm (table 1). Surface roughness gradually decreases from 1.7 to 0.88 nm, as shown in figures 5(g)–(j) and table 1. It is indicated that the increase of power is beneficial for the enhanced uniformity and reduction of surface roughness thanks to the increased ion flux in HiPIMS plasma to result in the improved diffusion of adsorbed atoms [4, 17, 20]. Surface morphologies of TiSiCN nanocomposite coatings deposited on Si substrates are further investigated by FESEM and TEM images (figure 6). As shown in figures 6(a)–(c), trilayer coatings consist of Ti, TiSiC and TiSiCN layers, which possess smooth morphologies and dense microstructure. It is confirmed by TEM images that trilayer coatings have dense interfaces between each layer in figures 6(d), (e). The constant thickness of Ti and TiSiC layers are 1.1 μm and 0.4 μm, respectively. The selected area electron diffraction inserted in figure 6(e) presents (111), (200) and (220) diffraction rings from cubic TiCN phase. Continuously bright diffraction rings reveal grain size in nanoscale. HRTEM images exhibit the nanocomposite structure with (111) and (200) oriented nc-TiCN embedded in amorphous matrix, and TiCN grain size is about 2–6 nm (figure 6(f)).

3.2. Mechanical properties and adhesion

Figure 7 shows hardness, Young's modulus, H/E^*, H^3/E^{*2} and HRC adhesion of TiSiCN nanocomposite coatings. It is defined that the toughness of materials refers to the ability of a material to absorb energy during deformation up to fracture. H/E^* and H^3/E^{*2} ratios of hard coatings are related to the resistance of elastic strain to failure and plastic deformation. Hence, H/E^* and H^3/E^{*2} ratios are found to have a strong relationship with toughness of hard coatings [4, 16, 24]. As shown in figure 7(a), hardness and Young's modulus gradually increase from 35.3 GPa and 325 GPa at 4 kW to 43 GPa and 359 GPa at 8 kW, respectively, benefited from the combined contributions of dense nanocomposite structure and refined nanograins. However, H/E^* and H^3/E^{*2} show an initial increase from 0.11 and 0.421 at 4 kW to 0.122 and 0.63 at 7 kW, and followed by a decrease to 0.19 and 0.61 at 8 kW (figure 7(b)). Li *et al* [33] deposited superhard TiSiCN coating on Ti6Al4V by arc ion plating with a hardness of 43.6 GPa, H/E of 0.103 and H^3/E^2 of 0.46. The coating presents coarse columnar crystal structure. Wang *et al* [28] and Abd El-Rahman *et al* [34] found that the enhanced hardness and toughness of TiSiCN coatings resulted from the structural transformation from columnar crystal to nanocrystalline. TiSiCN coatings with the combination of the highest H^3/E^{*2} of 0.285 and the hardness of 39.8 GPa were achieved by arc ion plating depositions. It is noted that TiSiCN coating with coarse columnar crystal structure deposited by multi arc

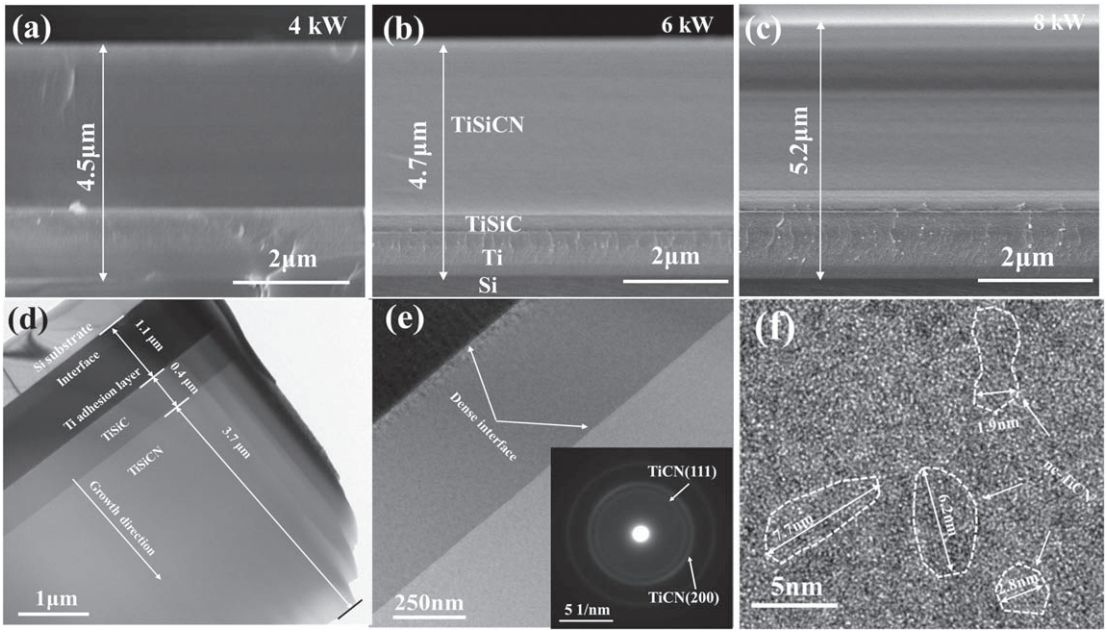

Figure 6. (a)–(c) FESEM and (d)–(f) TEM images of TiSiCN nanocomposite coatings deposited on Si substrates by HiPIMS at 8 kW.

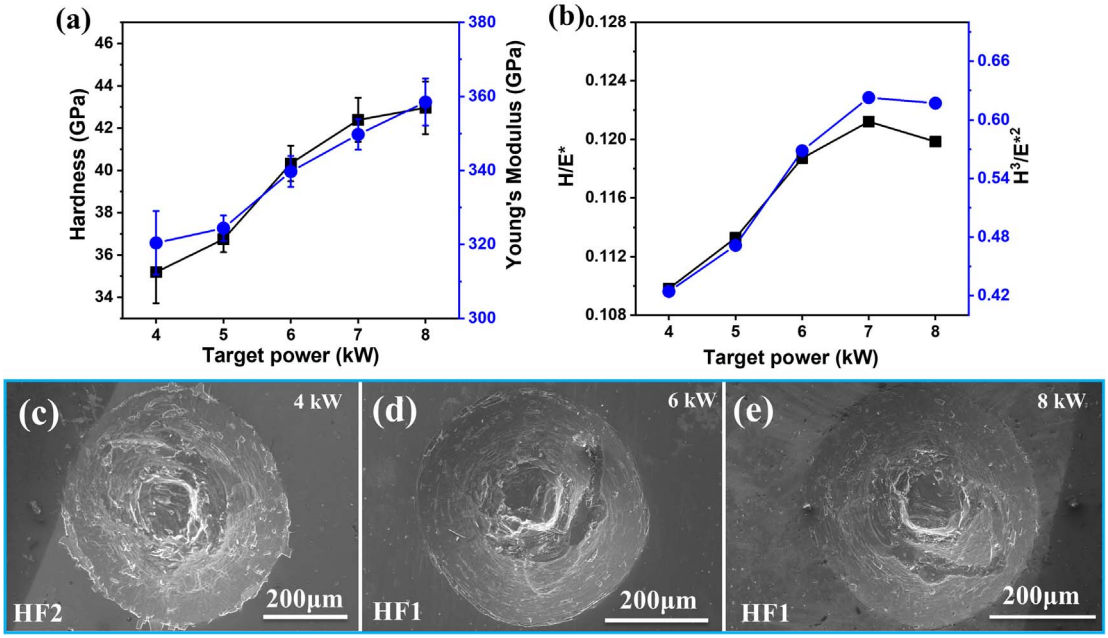

Figure 7. Hardness, Young's modulus, (b) H/E^*, H^3/E^{*2} and (c) HRC adhesion of TiSiCN nanocomposite coatings.

ion plating also shows a low H/E (<0.07) and H^3/E^{*2} (<0.12) with a hardness of 30 GPa [35]. It is suggested that H/E or H/E^* ratio is related to the elastic deformation and plastic deformation of coating under stress, a high H/E or H/E^* ratio leads to a high elastic strain before plastic deformation [36, 37]. Hence, the increased H/E^* and H^3/E^{*2} ratio can effectively improve the fracture toughness of the coatings [38]. In our case, TiSiCN coating with high H/E^* and H^3/E^{*2} ratio was prepared by HiPIMS, indicating the enhanced toughness of the superhard coatings due to the amorphous/nanocrystalline structure free of defects. The slight decrease of H/E^* and H^3/E^{*2} is related to the increased grain size under a strong ion flux of HiPIMS plasma at higher power. It is found that appropriate enhancement in ion energy of HiPIMS plasma is beneficial for the formation of high surface/interface integrity and dense microstructure, leading to a significant improvement in H, H/E^* and H^3/E^{*2} of nanostructured coatings [4, 16, 17].

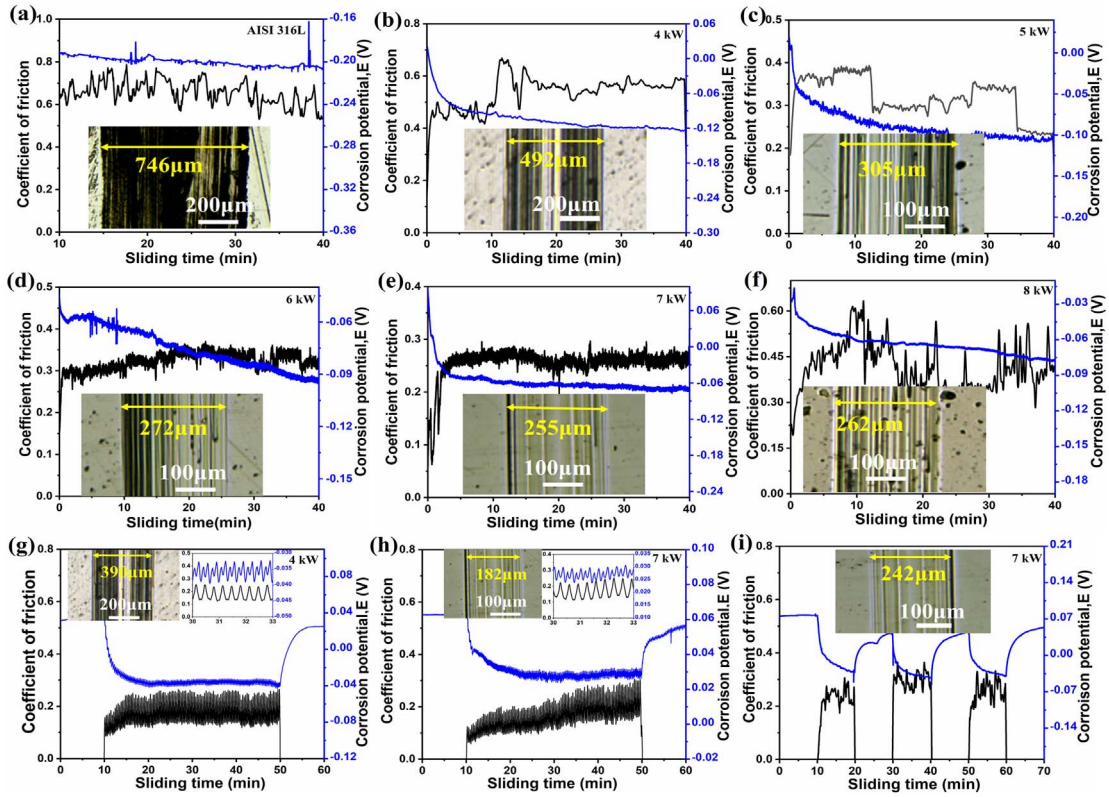

Figure 8. COF and OCP of TiSiCN nanocomposite coatings deposited by HiPIMS at a power of 4–8 kW in 3.5 wt.% NaCl aqueous solution, as well as the images of worn surface inserted, as compared with those of AISI 316L stainless steel.

The adhesion of TiSiCN nanocomposite coatings deposited on AISI 316L stainless steel (soft substrate) was studied depending on Rockwell C indentations, which reveals the process of deformation along with that of soft substrate during loading-unloading. Figures 7(c)–(e) presents the FESEM images of Rockwell C indentations of coatings deposited by HiPIMS at a power of 4–8 kW. At 4 kW, coatings have HRC adhesion of HF2 due to visible delamination and radial cracks at the edge of Rockwell C indentation. It is found that the increasing power enhances the adhesion up to HF1 at 8 kW. The issue of adhesion of tribological hard coatings plays a key role in wear, corrosion and tribocorrosion resistance [24, 31, 32]. One of the key problems is how to control residual stress state at coating/substrate interfaces to build low relatively stable stress coatings by the method of high ion flux plasma with low ion energy. In our case, TiSiCN/TiSiC/Ti trilayer coatings were designed to obtain high adhesion strength under the optimized HiPIMS plasma conditions to achieve low residual stress by chemical composition and trilayer structure as well as dense interfaces.

3.3. Tribocorrosion behaviors in 3.5 wt.% NaCl aqueous solution

Tribocorrosion is a complex process coupled with wear and corrosion in aggressive medium to result in the acceleration of deterioration of materials. Hence, it is will be a good strategy to enhance tribocorrosion properties by the method of novel material designs and advancing preparation techniques. Moreover, *in situ* electrochemical response based on the change of open circuit potential (OCP), the variation of coefficient of friction (COF) and worn surface morphologies are used to explore tribocorrosion mechanism. Figure 8 presents COF and OCP of TiSiCN nanocomposite coatings deposited by HiPIMS at a power of 4–8 kW varied with sliding time in 3.5 wt.% NaCl aqueous solution, as well as the images of worn surface inserted, as compared with those of AISI 316L stainless steel. The normal load of 1 N and reciprocating frequency of 1 Hz are used in figures 8(a)–(f). The fluctuation of COF and OCP are obtained for AISI 316L stainless steel substrates due to severe abrasive wear and simultaneous corrosion damage. The values of COF and OCP are 0.7 and −0.20 V, respectively. A large amount of black debris is covered on wear track with 746 μm in width, as shown in figure 8(a).

The fluctuate of OCP value usually is related to various factors including the electrochemical condition of working electrode, sliding contact surface, mass transfer, and competitive effects of applied potential and film dissolution rate [39–42]. During sliding wear in 3.5 wt.% NaCl aqueous solution, passive films are subjected to the continuous formation and breaking, which has a close correlation with the change of OCP. As shown in

figures 8(a)–(f), The tribocorrosion process of TiSiCN film in 3.5 wt.% NaCl aqueous solution can be divided into two different stages of rapid descent section and relatively stable section. Rapid descent section corresponds to the destruction of passivation film, followed by a relatively stable section corresponding to the dynamic equilibrium stage of mechanical depassivation and electrochemical repassivation. In addition, the OCP of the coatings decreases slowly in relatively stable sections probably due to the increasing wear tracks [28, 39]. The OCP value in stable section increases from −0.12 to −0.06 V with increasing average power from 4 to 7 kW, higher than −0.20 V for AISI 316L stainless steel. At 8 kW, the coatings shows a slight decrease of OCP (−0.08 V). The OCP of coatings increases along with the decrease of worn surface width. This may be attribute to the increase of low-energy ion bombardment flux in the deposition process with the increase of target power, which improves the densification of the coating and leads to the increase of corrosion resistance. However, with the target power increase to 8 kW, the ion sputtering effect associated with ion bombardment leads to the increase of defect concentration in the coating result in the decrease of corrosion resistance. In addition, target power also affects the OCP of the coating by affecting the hardness and toughness of the coating and controlling the width of the wear mark. Therefore, TiSiCN nanocomposite coatings deposited on AISI 316L stainless steel exhibit excellent tribocorrosion resistance. It is observed that there is a relaxation process of passive films during complex tribocorrosion. Hence, a higher load (10 N) under a slow sliding speed (0.05 Hz) was carried out to explore passive film behavior by the change OCP revealing *in situ* electrochemical response. Figures 8(g)–(h) exhibits changes of COF and OCP of TiSiCN nanocomposite coatings deposited at 4 and 7 kW under 10 N and 0.05 Hz. Both COF and OCP show an oscillation tendency, and they are corresponding to each other. The value of COF, OCP and width of wear track are 0.2, 0.03 V and 255 μm at 7 kW, better than 0.25, −0.04 V and 492 μm at 4 kW. The fluctuations of the OCP of TiSiCN coatings during sliding are due to repetitive passivation influenced by the ratio of active and passive region on worn surface. The rate of electrochemical repassivation exceeds mechanical depassivation, which would result in increasing OCP. Otherwise, the rate of the mechanical depassivation exceeding the electrochemical repassivation leads to the decrease of OCP [43]. The increased COF reveals the increase of plastic micro-cutting force, resulting in the elimination of passive films. On the contrary, when COF gradually decrease, passive films would form as soon as possible. The difference between the rise of COF and the fall of OCP is related to the ball motion mode of linear reciprocating tribometer. After the sliding, the OCP value increases gradually into initial value because of fast electrochemical repassivation. The fast electrochemical repassivation ability originate from high density grain boundary in TiSiCN nanocomposite coatings. The atoms at the grain boundary or the interface between amorphous and nanocrystalline are in metastable state, which can provide a large number of electrochemical active sites [44, 45]. The OCP value changes from the first cycle to the third cycle show a smooth feature without a sudden change, indicating stable and mild tribocorrosion process of TiSiCN nanocomposite coatings.

In order to understand the mechanism of tribocorrosion of the TiSiCN nanocomposite coatings in 3.5% NaCl aqueous solution, SEM images of the wear trace were shown in figure 9. EDS results of typical morphology in SEM images were taken as presented in table 2. The samples were taken out from the 3.5 wt.% NaCl aqueous solution and dried, and then sent to the vacuum chamber for SEM observation. All samples exhibits a rough worn surface with parallel grooves covered by a few flakes and granular debris. Big cubic particles formed on worn surface are determined as sodium chloride crystallization.

The wear mechanism of TiSiCN nanocomposite coating is dominated by the combined abrasive and adhesive wear. In contrast to other TiSiCN coatings with low H/E^* and low H^3/E^{*2}, there are no micro cracks or tiny corrosion spot worn surface after careful observation (figure 9). This can be attributed to the high toughness and high adhesion between coatings and substrates of TiSiCN coatings. There are a lot of microcracks or peeling off on the worn surface of TiSiCN coatings with with low H/E^* and low H^3/E^{*2} in air or simulated seawater environment [28, 34, 35]. In general, coatings cracking is fatigue caused under cyclic loading in reciprocating sliding tests. It has been well known that surface defects and porous microstructure and interfaces always offer ion channels for Cl^- penetration to cause delamination of coatings [4, 6, 7, 11, 24, 46]. The accumulation of Cl^- at the microcracks accelerates the corrosion and promotes the propagation of the cracks. The development of microcracks leads to the cracking and peeling off of coatings. High toughness coating can inhibit the formation of microcracks, and then inhibit pitting. On the one hand, the low microdefect density of $TiCN/Si_3N_4$ nanocrystalline-amorphous composite structure in TiSiCN coating can inhibit the nucleation of microcracks, on the other hand, the propagation of microcracks in the coating is hindered by the high-density irregular grain boundaries in $TiCN/Si_3N_4$ composite structure, resulting in energy dissipation, which limits the microcracks caused by external stress to a very small area. In addition, high values of H, H/E^*, H^3/E^{*2} of coatings promote cooperative deformation of overall coating/substrate system beneficial for the increase of cracking resistance of the coatings during tribocorrosion tests [13, 28]. Thus, TiSiCN coating with the enhanced toughness prevents Cl^- pitting by restraining micro cracks during abrasive wear. These features reveal that TiSiCN nanocomposite coatings have excellent tribocorrosion resistance without pitting corrosion induced by chloride during sliding wear in 3.5 wt% NaCl aqueous solution.

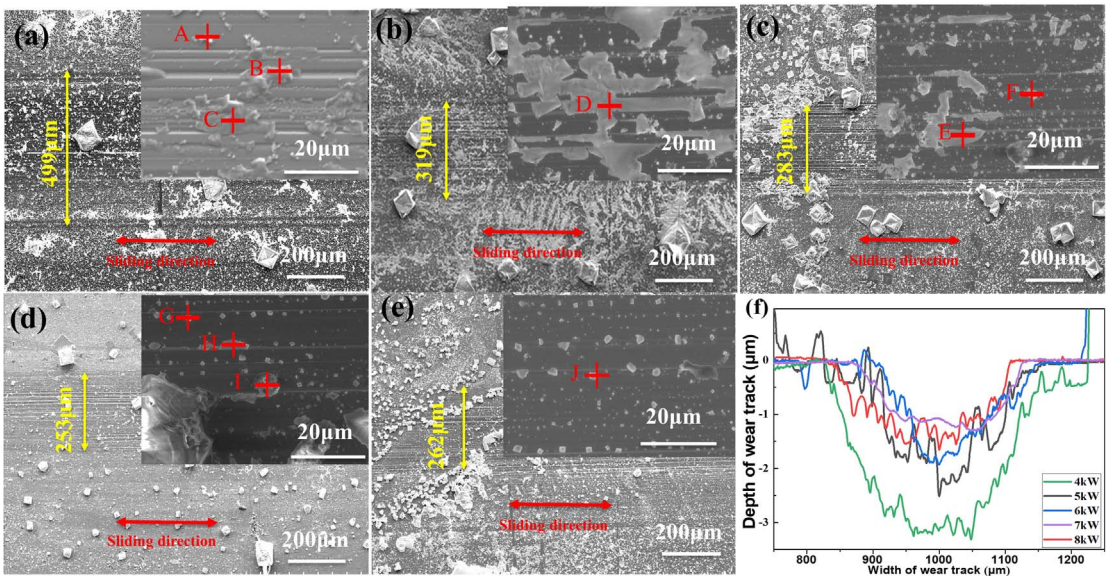

Figure 9. SEM images and 2D profiles of wear track of TiSiCN nanocomposite coatings sliding against Si_3N_4 balls in 3.5 wt.% NaCl aqueous solution: (a) 4 kW, (b) 5 kW, (c) 6 kW, (d) 7 kW, (e) 8 kW, (f) 2D profiles of wear surface.

Table 2. EDS results of the TiSiCN nanocomposite coatings after tribocorrosion test.

Point	Ti(at.%)	Si(at.%)	C(at.%)	N(at.%)	O(at.%)
A	20.34	7.30	21.15	42.04	9.17
B	31.73	15.21	52.94	0.11	—
C	46.23	16.27	22.80	—	14.69
D	12.40	5.58	12.46	8.12	61.44
E	32.29	12.23	31.90	23.58	—
F	25.67	10.30	23.61	23.13	17.29
G	18.12	6.99	13.85	10.36	50.69
H	28.21	7.78	21.89	31.03	11.09
I	13.55	5.12	18.35	—	62.97
J	23.80	9.22	25.76	27.79	13.44

Table 2 presents the elements content proportion of worn surface with smooth feature in EDS results ignored the Na and Cl element. EDS results (point C, D and I) show that flake debris contain much higher O contents (>14 at.%) than XPS data (<3 at.%), indicating oxidative wear mechanism. The composition of most granular debris (point A, F, G and J) was similar to that of TiSiCN nanocomposite coatings, which is mainly caused by the accumulation of debris produced by hard abrasive debris ascribed to abrasive wear mechanism. There is fewer N signal at point B, C, I in EDS results, suggesting interphase corrosion.

When TiSiCN nanocomposite coatings were deposited at 7 kW (figure 9), wear and corrosion debris on worn surface of coatings become less due to the reduction of plastic micro-cutting in abrasive wear as compared to that of 4 kW. Thus, COF gradually reaches a stable wear process with a value of 0.26 and OCP possesses a stable tendency of about −0.06 V. Width of wear track sharply decreases to 255 μm. Moreover, there is a leveling-off for changes in both COF and OCP. However, at 8 kW, the coating shows the fluctuation of COF and the slight decrease of OCP. Meanwhile, severe abrasive wear is occurred to produce deep furrows and increasing debris and width of wear track. The calculated specific tribocorrosion rate decrease from 1.54×10^{-4} to 4.78×10^{-5}, lower than that of 7.28×10^{-4} mm^3 N^{-1} m^{-1} for AISI 316L stainless steel substrate (table 1). Compared with TiSiCN coating prepared by other methods, the uniform wear properties of the high-toughness TiSiCN coating deposited by HiPIMS avoid coatings failure caused by local cracks [28, 34, 35]. Although there are no significantly decreases of the wear rate on TiSiCN coatings deposited by HiPiMS, it still has better application value.

The deep grooves covered by a large amount of wear debris are observed on the coatings deposited by 4 kW due to relative low H, H/E^*, H^3/E^{*2} ratios, indicating low hardness and toughness [13] of the coatings, which has high COF of 0.55 and low OCP value of −0.12 V in tribocorrosion process. Hard abrasive usually has a

strong cutting effect on sliding contact surface. However, flake oxidation wear debris accumulates in groove would act as a lubricating in tribocorrosion process [42, 47–49]. The deep groove hinders the accumulation of oxide wear debris, thus weakens the lubrication effect of oxide wear debris. As target power is increased to 7 kW (figures 8 and 9), there is a significant enhancement in tribocorrosion properties with the decrease of COF to 0.26 and the increase of OCP to −0.07 V thanks to high H, H/E^* and H^3/E^{*2}. At 7 kW, indeed, fewer tiny debris is covered and only shallow furrows are observed on the smooth worn surface. The width of the wear track is 255 μm. That indicates the transition of the tribocorrosion mechanism from severe abrasive wear to mild abrasive wear.

Therefore, the enhanced tribocorrosion properties of TiSiCN nanocomposite coatings mainly depended on the combined improvements in hardness and toughness of TiSiCN nanocomposite coatings with high surface integrity and dense microstructure, which promotes the resistance of microcrack and corrosion damage. The tribocorrosion mechanism of TiSiCN nanocomposite coatings in 3.5 wt.% NaCl aqueous solution were oxidative wear mechanism and abrasive wear mechanism. It transformed from severe abrasive wear to mild abrasive wear with the combined improvements in hardness and toughness. Moreover, cycling tribocorrosion tests exhibited that passive films of coatings have strong abilities of regeneration and repairation on sliding contact surface to protect the coatings from the exposure to the corrosive solution. Thus, the sharp decrease of COF below 0.2 at a lower sliding speed is obtained for of the coatings deposited at 7 kW possibly resulted from self-lubricating properties of passive films and surface feature of the coatings.

4. Conclusion

(1) TiSiCN nanocomposite coatings were deposited by high power impulse magnetron sputtering (HiPIMS) at a power of 4–8 kW, where metal Ti and TiSiC layers serve as adhesion and transition layers, respectively. Trilayer coatings present high surface/interface integrity and dense microstructure. As power is increased, TiSiCN nanocomposite coatings possess *nc*-(TiN, TiC, TiCN)/*a*-(Si_3N_4, SiC, sp^2–C) nanocomposite structure without distinctly preferred orientation. The residual stress in the coatings increased from −1.13 to −2.13 GPa with the power rise from 4 to 8 kW.

(2) The highest hardness (H) of 43 GPa and effective Young's modulus (E^*) of 360 GPa are achieved at 8 kW, while the highest H/E^* of 0.123 and H^3/E^{*2} of 0.61 appear at 7 kW. Rockwell C adhesion level of coatings is improved from HF2 at 4 kW to HF1 at 8 kW. TiSiCN nanocomposite coatings with high H, H/E^*, H^3/E^{*2} and adhesion strength exhibit high open circuit potential of −0.07 V, low COF of 0.25 and specific wear rate of 4.78×10^{-5} mm^3 N^{-1} m^{-1} resulting from mild abrasive wear without the occurrence of pitting corrosion in 3.5 wt.% NaCl aqueous solution.

(3) The tribocorrosion mechanism of TiSiCN nanocomposite coatings in 3.5 wt.% NaCl aqueous solution are oxidative wear mechanism and abrasive wear mechanism. It transformed from severe abrasive wear to mild abrasive wear with the combined improvements in hardness and toughness. Moreover, cycling tribocorrosion tests exhibit that passive films of coatings have strong abilities of regeneration and self-repairation on sliding contact surface to protect the coatings from the exposure to the corrosive solution.

Acknowledgments

This work was supported by National Science and Technology Major Project (Grant No. 2017-VII-0012-0108), Guangdong Province Key Area Research and Development Program (Grant No. 2019B090909002) and 2020 talent plan granted by Beijing Academy of Science and Technology.

Data availability statement

The data of this study are available from the correspondsing authors upon reasonable requests.

Declarations of interest

There are no conflicts to declare.

ORCID iDs

Yixiang Ou https://orcid.org/0000-0001-9889-4222

References

[1] Husain E *et al* 2013 Marine corrosion protective coatings of hexagonal boron nitride thin films on stainless steel *ACS Appl. Mater. Interfaces* **5** 4129–35
[2] Wood R J K 2017 Marine wear and tribocorrosion *Wear* **376–377** 893–910
[3] Sui X *et al* 2018 Tailoring the tribocorrosion and antifouling performance of (Cr, Cu)-GLC coatings for marine application *ACS Appl. Mater. Interfaces* **10** 36531–9
[4] Ou Y X *et al* 2015 Wear and corrosion resistance of CrN/TiN superlattice coatings deposited by a combined deep oscillation magnetron sputtering and pulsed dc magnetron sputtering *Appl. Surf. Sci.* **351** 332–43
[5] Landolt D *et al* 2001 Electrochemical methods in tribocorrosion: a critical appraisal *Electrochim. Acta* **46** 3913–29
[6] Lei S *et al* 2016 Tribocorrosion behaviors of PVD CrN coated stainless steel in seawater *Wear* **362–363** 97–104
[7] Li L *et al* 2018 Enhanced tribocorrosion performance of Cr/GLC multilayered films for marine protective application *ACS Appl. Mater. Interfaces* **10** 13187–98
[8] Wang Y X *et al* 2014 Interlayer design for the graphite-like carbon film with high load-bearing capacity under sliding-friction condition in water *Appl. Surf. Sci.* **311** 816–24
[9] Cui G J *et al* 2012 Tribological properties of bronze–graphite composites under sea water condition *Tribol. Int.* **53** 76–86
[10] Wood R J K 2007 Tribo-corrosion of coatings: a review *J. Phys.* D **40** 5502
[11] Fu Y Q *et al* 2020 Electrochemical and tribocorrosion performances of CrMoSiCN coating on Ti-6Al-4V titanium alloy in artificial seawater *Corros. Sci.* **165** 108385
[12] Matthews A, Franklin S E and Holmberg K 2007 Tribological coatings: contact mechanisms and selection *J. Phys.* D **40** 5463
[13] Ou Y X *et al* 2020 Hard yet tough CrN/Si_3N_4 multilayer coatings deposited by the combined deep oscillation magnetron sputtering and pulsed dc magnetron sputtering *Appl. Surf. Sci.* **502** 144168
[14] Buchinger J *et al* 2019 Toughness enhancement in TiN/WN superlattice thin films *Acta Mater.* **172** 18–29
[15] Yalamanchili K *et al* 2015 Tuning hardness and fracture resistance of ZrN/$Zr_{0.63}Al_{0.37}N$ nanoscale multilayers by stress-induced transformation toughening *Acta Mater.* **89** 22–31
[16] Ou Y X *et al* 2018 Microstructure and tribological behavior of TiAlSiN coatings deposited by deep oscillation magnetron sputtering *J. Am. Ceram. Soc.* **101** 5166–76
[17] Lin J *et al* 2011 Recent advances in modulated pulsed power magnetron sputtering for surface engineering *JOM* **63** 48–58
[18] Kuprin A S *et al* 2015 Vacuum-arc chromium-based coatings for protection of zirconium alloys from the high-temperature oxidation in air *J. Nucl. Mater.* **465** 400–6
[19] Shen M L *et al* 2015 High vacuum arc ion plating NiCrAlY coatings: microstructure and oxidation behavior *Corros. Sci.* **94** 294–304
[20] Anders A 2017 Tutorial: reactive high power impulse magnetron sputtering (R-HiPIMS) *J. Appl. Phys.* **121** 171101
[21] Machunze R *et al* 2009 Stress and texture in HIPIMS TiN thin films *Thin Solid Films* **518** 1561–5
[22] Oliveira J C *et al* 2018 Reduced atomic shadowing in HiPIMS: Role of the thermalized metal ions *Appl. Surf. Sci.* **433** 934–44
[23] Loquai S *et al* 2016 Flash post-discharge emission in a reactive HiPIMS process *Appl. Phys. Lett.* **109** 114101
[24] Ou Y X *et al* 2019 Tribological behaviors in air and seawater of CrN/TiN superlattice coatings irradiated by high-intensity pulsed ion beam *Ceram. Int.* **45** 24405–12
[25] Lin J *et al* 2010 The structure and mechanical and tribological properties of TiBCN nanocomposite coatings *Acta Mater.* **58** 1554–64
[26] Lauridsen J *et al* 2010 Microstructure evolution of Ti–Si–C–Ag nanocomposite coatings deposited by DC magnetron sputtering *Acta Mater.* **58** 6592–9
[27] Yao Y *et al* 2015 Influence of the negative bias in ion plating on the microstructural and tribological performances of Ti–Si–N coatings in seawater *Surf. Coat. Technol.* **280** 154–62
[28] Yue W *et al* 2017 Influence of carbon contents on the structure and tribocorrosion properties of TiSiCN coatings on Ti6Al4V *Tribol. Int.* **109** 285–96
[29] Thangavel E *et al* 2013 Synthesis and characterization of Ti–Si–C–N nanocomposite coatings prepared by a filtered vacuum arc method *Appl. Surf. Sci.* **265** 60–5
[30] Stüber M *et al* 2002 Microstructure and properties of low friction TiC-C nanocomposite coatings deposited by magnetron sputtering *Surf. Coat. Technol.* **150** 218–26
[31] Jo Y J *et al* 2018 Synthesis and electrochemical properties of Ti-doped DLC films by a hybrid PVD/PECVD process *Appl. Surf. Sci.* **433** 1184–91
[32] Hatem A *et al* 2018 Tribocorrosion behavior of low friction TiSiCN nanocomposite coatings deposited on titanium alloy for biomedical applications *Surf. Coat. Technol.* **347** 1–12
[33] Li J L *et al* 2017 Structure and tribological properties of TiSiCN coating on Ti6Al4V by arc ion plating *Thin Solid Films* **644** 115–9
[34] Abd El-Rahman A M and Wei R 2014 Effect of ion bombardment on structural, mechanical, erosion and corrosion properties of Ti–Si–C–N nanocomposite coatings *Surf. Coat. Technol.* **258** 320–8
[35] Dong M *et al* 2019 Structure and tribocorrosion properties of duplex treatment coatings of TiSiCN/nitride on Ti6Al4V alloy *Ceram. Int.* **45** 12461–8
[36] Leyland A and Matthews A 2000 On the significance of the H/E ratio in wear control: a nanocomposite coating approach to optimised tribological behaviour *Wear* **246** 1–11
[37] Leyland A and Matthews A 2004 Design criteria for wear-resistant nanostructured and glassy-metal coatings *Surf. Coat. Technol.* **177–178** 317–24
[38] Matthews A, Franklin S and Holmberg K 2007 Tribological coatings: contact mechanisms and selection *J. Phys. D: Appl. Phys.* **40** 5463
[39] Stojadinovic J *et al* 2009 Effect of electrode potential on the tribocorrosion of tungsten *Tribol. Int.* **42** 575–83
[40] Landolt D, Mischler S and Stemp M 2001 Electrochemical methods in tribocorrosion: a critical appraisal *Electrochim. Acta* **46** 3913–29
[41] Fathollahzade N and Raeissi K 2014 Electrochemical evaluation of corrosion and tribocorrosion behaviour of amorphous and nanocrystalline cobalt–tungsten electrodeposited coatings *Mater. Chem. Phys.* **148** 67–76
[42] Li D J, Guruvenket S and Klemberg-Sapieha J E 2011 Corrosion and tribo-corrosion enhancement of SS301 and Ti–6Al–4V substrates by amorphous hydrogenated SiN/SiC/a-C multilayer coating architecture *Surf. Coat. Technol.* **206** 1893–8

[43] Ou Y X et al 2016 Structure, adhesion and corrosion behavior of CrN/TiN superlattice coatings deposited by the combined deep oscillation magnetron sputtering and pulsed dc magnetron sputtering *Surf. Coat. Technol.* **293** 21–7
[44] Balyanov A et al 2004 Corrosion resistance of ultra fine-grained Ti *Scripta. Mater.* **51** 225–9
[45] Li W and Li D Y 2005 Variations of work function and corrosion behaviors of deformed copper surfaces *Appl. Surf. Sci.* **240** 388–95
[46] Shao T et al 2018 Microstructural effect on the tribo-corrosion behaviors of magnetron sputtered CrSiN coatings *Wear* **416–417** 44–53
[47] Shan L et al 2016 Tribocorrosion behaviors of PVD CrN coated stainless steel in seawater *Wear.* **362–363** 97–104
[48] Yamamoto K, Sato T and Takeda M 2005 Structural analysis of $(Cr_{1-x}Si_x)N$ coatings and tribological property in water environment *Surf. Coat. Technol.* **193** 167–72
[49] Wang Q Z et al 2011 Comparison of tribological properties of CrN, TiCN and TiAlN coatings sliding against SiC balls in water *Appl. Surf. Sci.* **257** 7813–20